Advanced Steel Construction – Vol. 21 No. 1 (2025) 73–82
DOI:10.18057/IJASC.2025.21.1.7

REPAIRING EFFECT OF DOUBLE-SIDED ARRAY STEEL-RODS REINFORCEMENT METHOD FOR U-RIB CRACKS

Cheng Meng, Zhi-Yuan Yuanzhou *, Bo-Hai Ji, Zhuang-Zhuang Chen and Jun-Yuan Xia

College of Civil and Transportation Engineering, Hohai University, Nanjing, Jiangsu, 210098, China

**(Corresponding author. Email: yz-zhiyuan@hhu.edu.cn)*

A B S T R A C T

U-rib cracks are one of the typical fatigue cracking modes in steel box girders. To address this issue, a double-sided reinforcement technique, incorporating microstructural damage by using steel rods and steel plates, was proposed. The mechanical performance of steel-rod reinforcement (SRR) and steel-rod plate reinforcement (SRPR) was evaluated using a series of compact tension-shear (CTS) specimens under varying loading angles. Subsequently, finite element models were employed to simulate and compare the maintenance effects of the two configurations. Finally, field application and monitoring were conducted on a U-rid long fatigue crack in a real bridge. The results indicated that both SRR and SRPR significantly improved the tensile strength, effectively reducing the KI at the crack tip, with SRPR exhibiting stronger shear resistance. Monitoring data collected before and after maintenance demonstrated that the proposed new methods reduced stress concentration at the crack tip, inhibiting fatigue crack propagation.

A R T I C L E H I S T O R Y

Received: 21 March 2024
Revised: 16 December 2024
Accepted: 16 December 2024

K E Y W O R D S

Steel-rod and steel plate;
Structural damage;
Fatigue crack;
Effect evaluation;
Field maintenance

1. Introduction

Fatigue cracking is one of the main failure modes in steel box girders, and it is becoming an increasing concern for engineers [1][2]. Under cyclic traffic loading, components of steel box girder are prone to fatigue cracking because of their complex structure and numerous weld details, as demonstrated by previous studies [3][4]. The propagation of these cracks has the potential to significantly compromise the safety and performance of steel box girders, leading to secondary diseases such as corrosion failure and pavement damage. As a result, there is a growing demand for effective repair methods to mitigate crack propagation and extend the lifespan of the structure.

Given the time and cost associated with component replacement, various temporary repair techniques have been developed and extensively studied by researchers to impede fatigue crack growth and enhance local capacity A cost-effective and efficient approach is to drill a smooth stop-hole at the crack tip, which eliminates eliminate plastic region and relieve the stress concentration thereat [5][6][7]. Although drilling stop-holes is simple and cost-effective, its effectiveness can be compromised by challenges such as accurately locating the crack tip and the potential for secondary crack propagation. Impact crack-closure retrofit treatment has been proposed and found to be effective by closing the crack surface in experiments and field maintenance [8][9]. The stress intensity factor reduced and the crack propagation was retarded, as the crack surface remains closed after this treatment, but the effect of impact crack-closure retrofit treatment on long cracks still needs further research [10]. Rewelding, following the removal of original cracks, is a common repair method but is constrained by specific operational environment requirements. In addition, the effects of rewelding are uncontrollable and influenced by complex factors [11][12], this leads to frequent secondary cracking, which complicates future maintenance. Bonding or bolting metal or composite plates and angles onto the crack surface can bear the load together with component and restrain long fatigue crack propagation effectively, but result in irreparable structural damage [13][14].

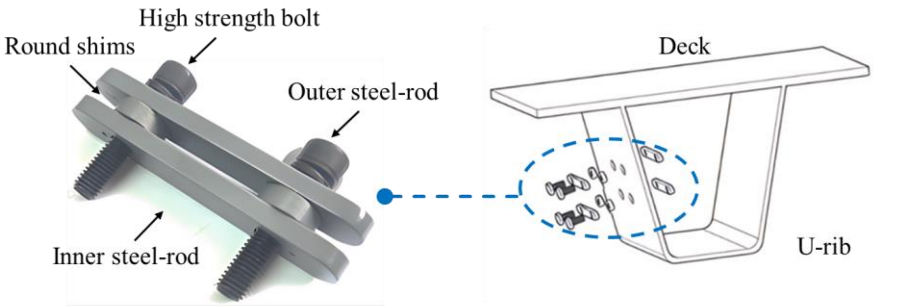

(a) Steel-rod reinforcement (SRR)

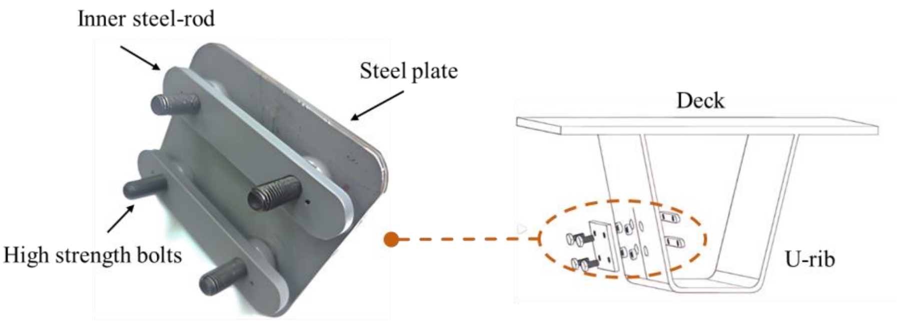

(b) Steel-rod-plate reinforcement (SRPR)

Fig. 1 Configurations of array steel-rod reinforcement

A significant challenge arises from the closure behaviour of U-ribs, which reduces the applicability of existing reinforcement methods for fatigue cracks in the U-rib. To minimize structural damage and prevent the introduction of new fatigue sources, a new array steel-rod reinforcement structure called SRR method was proposed for the U-rib web fatigue cracks [15]. This structure entailed the insertion of steel-rods into prefabricated holes within the U-rib, and connection either with steel-rods or steel plates on the outer side of the U-rib, thereby implementing double-sided reinforcement with micro structural damage, illustrated in Fig. **1**a. However, real bridge structures usually experience complicated loads, where the crack direction is not vertical to the applied loads. On this basis, another configuration employing steel-rods on the inner side and steel plates on the outer side is proposed in this work, which is termed steel-rod-plate reinforcement (short for SRPR), seen in Fig.1b. Further research is needed to evaluate the effectiveness of SRR and SRPR in practical bridge crack repair scenarios.

In this work, compact tension-shear (short for CTS) specimens were designed for conducting tension-shear mixed load tests [16]. The mechanical performance of SRR and SRPR was compared. Then, a segmental finite element model was simulated to evaluate the maintenance effects of these two reinforcement configurations. In addition, field maintenance and monitoring on a real steel bridge were carried out, the strain data near the crack tip before and after maintenance was recorded and the stress distribution was analyzed. The research results provide a reference for the repair of fatigue cracks subjected to mixed loads in real bridge applications.

2. Experimental investigations

2.1. Specimen

The CTS specimen was fabricated from Q345qD steel, which is widely used in the real bridge construction. The specific geometric details of the CTS specimen are given in Fig. **2**, and the size of specimens was 200 ×160 ×6 mm. Pre-existing edge cracks in the CTS specimens were introduced using wire electrical discharge machining, with a crack length of 80 mm and a width of 0.2 mm. For SRR, two pairs of steel rods were used, while SRPR adopted a combination of steel plate and inner steel-rods. The distance between steel-rods was 40 mm, and the steel plate with a size of 80×80 ×6 mm covered the crack.

The CTS fixtures, shown in Fig. **2**, were made from Q420 steel to apply a tension-shear mixed load at different angles (α). α = 0° corresponds to pure tension load, while α = 90° represents pure shear load. The application of pure tension load, pure shear load, as well as mixed-mode load was allowed to the CTS specimens simply by change α. The test conditions with different angles, loads and schemes are detailed in Table 1.

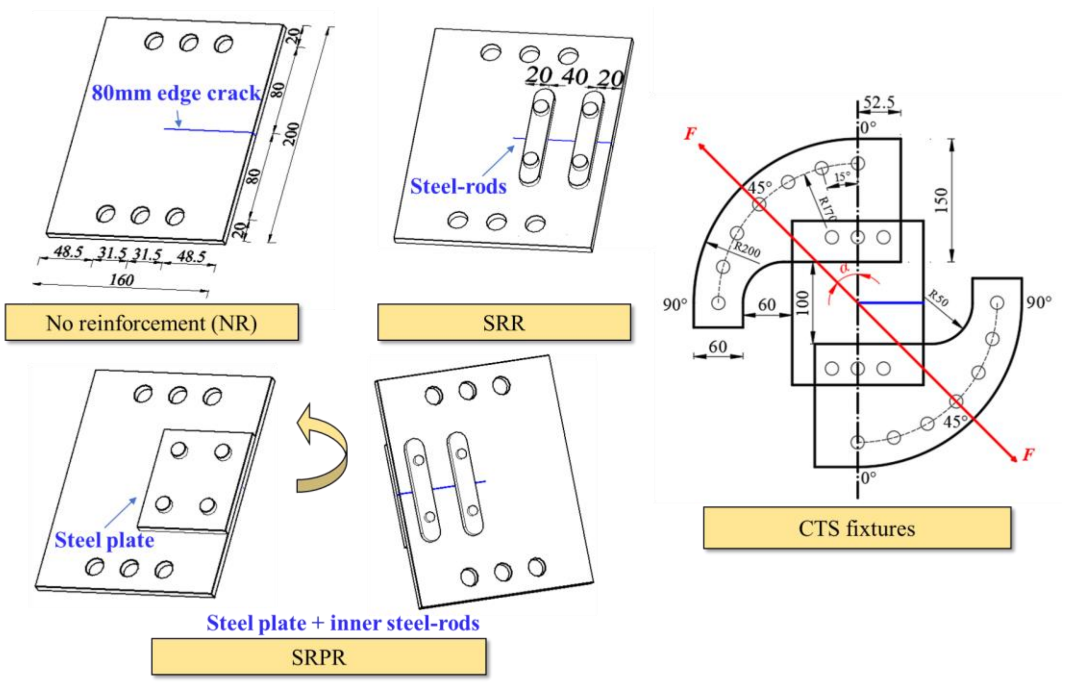

Fig. 2 Specimen details (Unit: mm)

Table 1
Test conditions

Specimen number	Angle α/°	Load /kN	Reinforcement scheme
SJ1			NR
SJ2	0	100	SRR
SJ3			SRPR
SJ4			NR
SJ5	45	70	SRR
SJ6			SRPR
SJ7			NR
SJ8	90	50	SRR
SJ9			SRPR

2.2. Experimental procedure

The test device is illustrated in Fig. **3**. Static tests were conducted using an electric universal testing machine with a maximum test force of 200 kN and an accuracy of ±0.5%. Steel-rods and steel plates were implemented on SRR and SRPR specimens. The high-strength bolts were pre-tightened to about 35N·m. Throughout the entire experimental procedure, the loading speed of the machine was stringently controlled at a steady loading rate of 2.0mm/min.

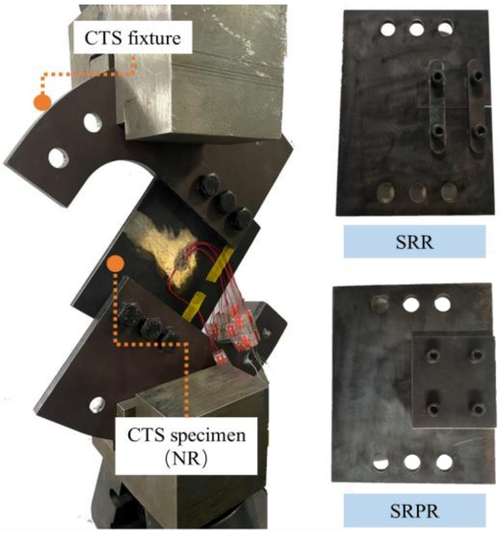

Fig. 3 Test device

To evaluate the effect of maintenance, strain gauges were strategically placed near the crack to analyze changes in the stress intensity factors. Rittel [17] proposed that the strains at any point located at (r, θ) can be expressed in a cartesian coordinate system (Fig. **4**a), donating by K_I and K_{II} the two stress intensity factors. Zhou et al. [18]investigated the influence of strain gauge position on the stress intensity factors and suggested a reasonable strain gauge arrangement for calculating the stress intensity factors. Fig. **4**b illustrates the arrangement of strain gauges on the specimen.

Where ε_{11} and ε_{22} are the strain measurements of the two strain gauges, E is the Young's modulus, here is 2.10×10^5 MPa. ν is the Poisson's ratio, here is 0.3.

$$\begin{aligned}
\varepsilon_{11} &= \frac{1}{E\sqrt{2\pi r_1}}\cos\frac{\theta_1}{2}\left[(1-\nu)-(1+\nu)\sin\frac{\theta_1}{2}\sin\frac{3\theta_1}{2}\right]K_I - \frac{1}{E\sqrt{2\pi r_1}}\sin\frac{\theta_1}{2}\left[2+(1+\nu)\cos\frac{\theta_1}{2}\cos\frac{3\theta_1}{2}\right]K_{II} \\
\varepsilon_{22} &= \frac{1}{E\sqrt{2\pi r_2}}\cos\frac{\theta_2}{2}\left[(1-\nu)-(1+\nu)\sin\frac{\theta_2}{2}\sin\frac{3\theta_2}{2}\right]K_I + \frac{1}{E\sqrt{2\pi r_2}}\sin\frac{\theta_2}{2}\left[2\nu+(1+\nu)\cos\frac{\theta_2}{2}\cos\frac{3\theta_2}{2}\right]K_{II}
\end{aligned} \tag{1}$$

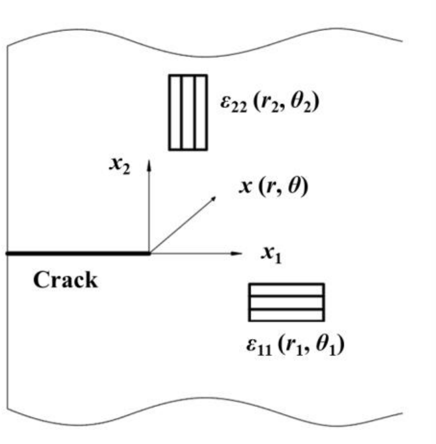

(a) Coordinate system

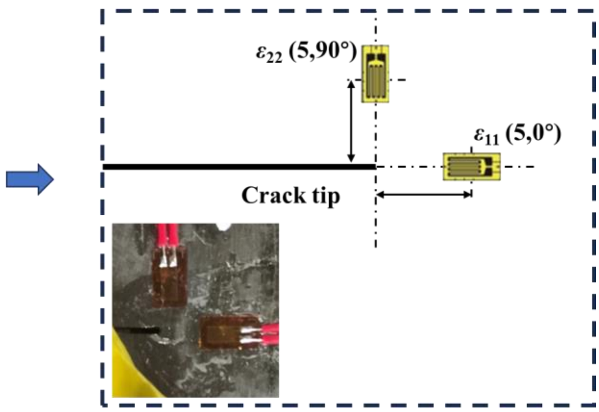

(b) Strain gauge positions

Fig. 4 Measurement points layout

2.3. Experimental results

2.3.1. Pure tension load

The stress intensity factors versus forces under pure tension load are presented in Fig. **5**. As the fracture toughness of Q345qD is 2 096 MPa·mm$^{1/2}$, the data exceeding 2 000 MPa·mm$^{1/2}$ have been omitted from the figure [19]. K_I exhibited a rapid increase as the applied load increased, while K_{II} remained consistently low and could be considered negligible. This behavior indicated that the specimens experienced a relatively uniform distribution of force, with the crack tip being subjected to approximately pure tension. The experimental load mode was close to the ideal uniaxial tension load. Both SRR and SRPR led to a reduction in the values of K_I. Notably, the presence of the steel plate resulted in a larger contact area, covering a greater portion of the effective crack length and restraining crack deformation, which led to a more significant decrease in K_I.

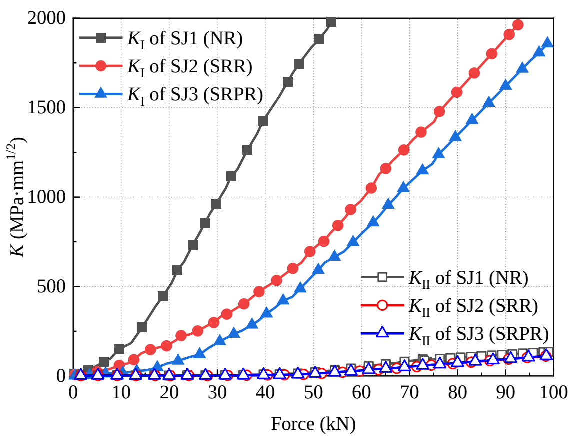

Fig. 5 The stress intensity factors under 0° (pure tension load)

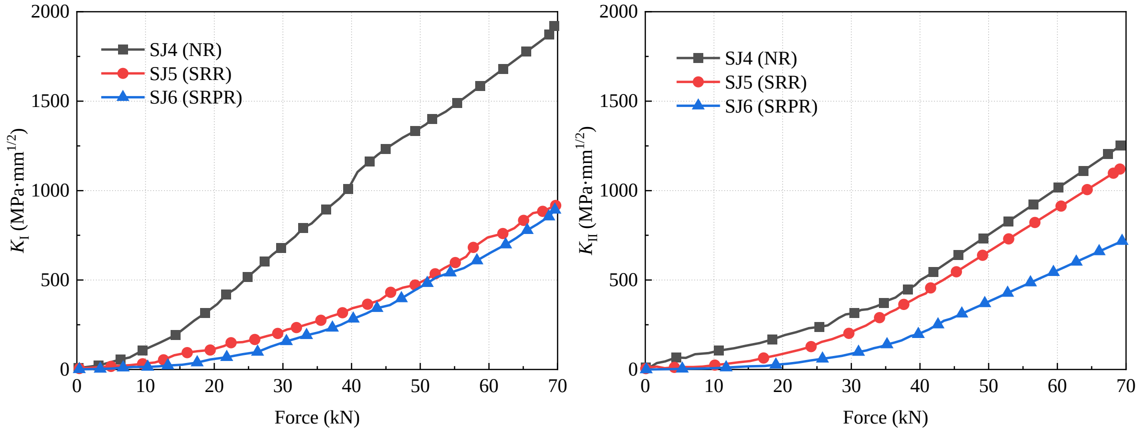

(a) K_I (b) K_{II}

Fig. 6 The stress intensity factors under 45° (tension-shear mixed load)

2.3.2. Tension-shear mixed load

Under tension-shear mixed load, the crack tip experienced tension and shear stresses simultaneously. As observed, K_I of SJ4 increased rapidly, while that of SJ5 and SJ6 exhibited slow growth. The reduction in K_I was approximately consistent for both the SRR and SRPR. K_{II} values, which remained relatively small, were minimally affected by SRR, as the trend of K_{II} curve growth of SJ4 and SJ5 was almost consistent. Benefiting by the steel plate, the shear resistance effect of SRPR was more obvious, manifested as K_{II} values of SJ6 reduced by a certain amount.

2.3.3. Pure shear load

As depicted in Fig. **7**, the pure shear load could be divided into two stages. When the load was small, K_I values were close to zero, indicating that the specimens were experiencing predominantly uniaxial shear stress. The K_{II} values decrease after maintenance. SRPR showed more reduction in the values of K_{II}. Once the load exceeded 38kN, both K_I and K_{II} exhibited a significant increased, which indicated that load mode has gradually shifted pure shear load to tension-shear mixed load. And the maintenance effect gradually decreased at this stage. The shear resistance of SRPR was slightly better.

At lower loads, both SRR and SRPR exhibited a certain shear resistance. As the external load increased, uniaxial pure shear load became unsustainable and turned to tension-shear mixed load with larger angles. SRPR demonstrated a more robust maintenance effect compared to SRR.

2.4. Stress analysis

2.4.1. Finite element model

The above experimental findings illustrated the effects of SRR and SRPR on reducing the stress intensity factors at the crack tip of CTS specimens under different loading angles. Numerical calculations were performed by using ABAQUS software to analyze the stress characteristics in these specimens. The loading condition was simplified to as a plane stress state and the specimens were assumed to be isotropic. The dimensions and material constants of the model were consistent with the specimens. The model was meshed using solid element type C3D8R with a grid size of 1mm, and the boundary conditions of the model are shown in Fig. **8**. The elastic modulus of the whole model was taken to be 2.06×10^5 MPa and the Poisson's ratio was 0.3.

The prefabricated crack was formed by extended finite element method and mesh refinement at the crack tip was conducted. In the models of specimens with SRR and SRPR, components such as steel-rods, steel plate, high-strength bolts and washers were modelled according to reference[15].To achieve loading at different angles, the external load was distributed according to the following equation [7].

$$\begin{aligned} F_1 &= F_6 = F\left(\frac{1}{2}\cos\alpha + \frac{m}{l}\sin\alpha\right) \\ F_2 &= F_5 = F\sin\alpha \\ F_3 &= F_4 = F\left(\frac{1}{2}\cos\alpha - \frac{m}{l}\sin\alpha\right) \end{aligned} \tag{2}$$

Where l and m are geometrical parameters, here are 80 mm and 62 mm respectively; α is the loading angle; F is the external load.

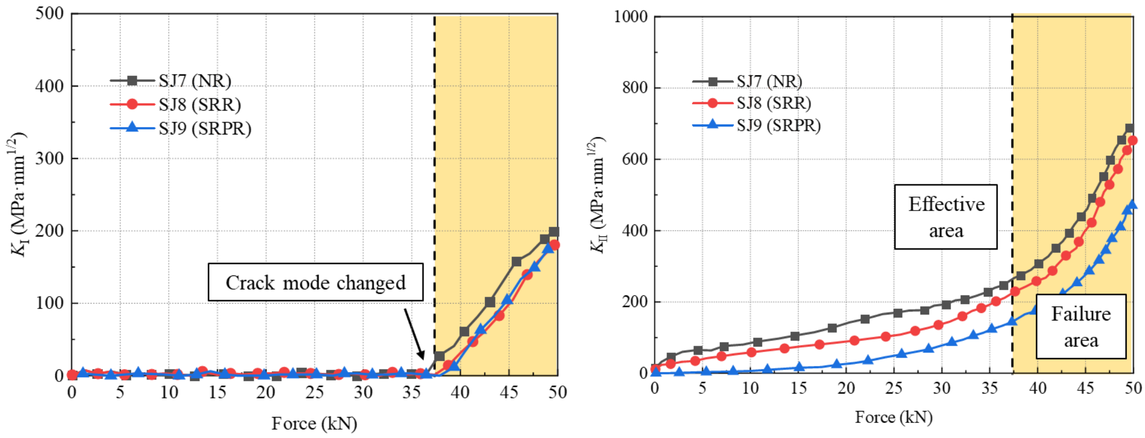

(a) K_I (b) K_{II}

Fig. 7 The stress intensity factors under 90° (pure shear load)

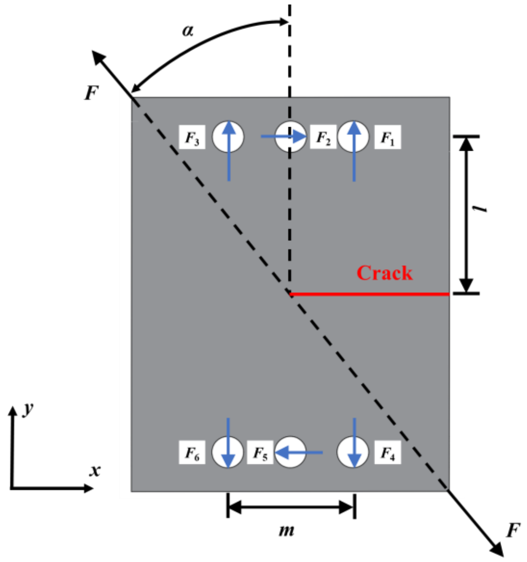

(a) Boundary conditions

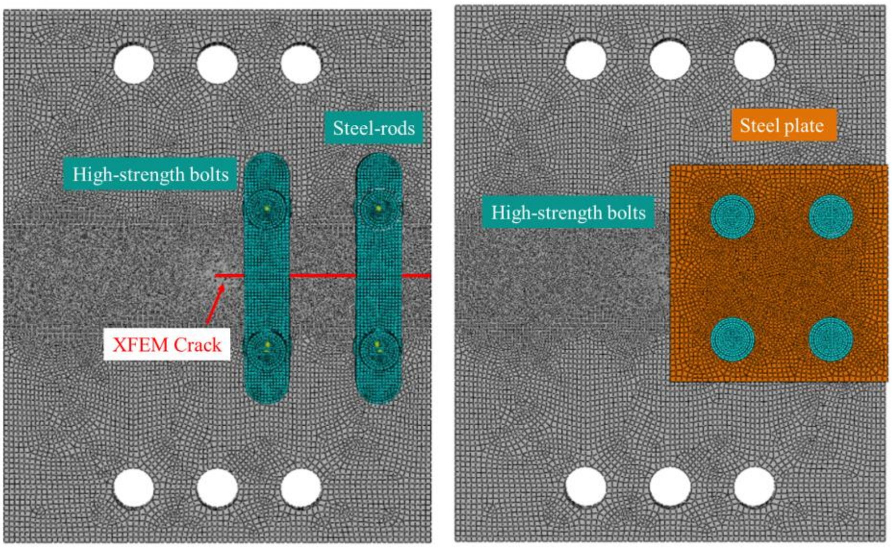

(b) Assembly and Meshing

Fig. 8 Finite element model (SRR and SRPR)

2.4.2. Model verification

For the NR specimens with edge crack, previous studies have provided a calculation method for the stress intensity factors at the crack tip [19], as shown in Eq. (3).

$$K_{\mathrm{I}}=\frac{F\cos\alpha}{Wt}\sqrt{\pi a}\frac{1}{(1-\frac{a}{W})}\sqrt{\frac{0.26+2.65(\frac{a}{W-a})}{1+0.55(\frac{a}{W-a})-0.08(\frac{a}{W-a})^2}}$$

$$K_{\mathrm{II}}=\frac{F\sin\alpha}{Wt}\sqrt{\pi a}\frac{1}{(1-\frac{a}{W})}\sqrt{\frac{-0.23+1.4(\frac{a}{W-a})}{1-0.67(\frac{a}{W-a})+2.08(\frac{a}{W-a})^2}} \quad (3)$$

Where a is the crack length, here is 80 mm; W and t are the width and the thickness of CTS specimen, here are 160 mm and 6 mm respectively.

Taking the model of NR specimen under a load of 40kN, the stress intensity factors K_{I} and K_{II} at the crack tip with different loading angles were calculated. And the theoretical results were obtained by Eq. (3), seen in Table 2. As shown, the error between the numerical results and theoretical results was within 6%, indicating the rationality and feasibility of the finite element model and loading form.

Table 2
Comparisons of stress intensity factors obtained by numerical and theoretical methods

Loding angle α /°	Stress intensty factors	Numerical results / MPa·mm$^{1/2}$	Theoretical results / MPa·mm$^{1/2}$	Error /%
0	K_{I}	904.2	929.4	2.71
	K_{II}	25.5	0	/
45	K_{I}	626.1	657.2	4.73
	K_{II}	343.8	325.4	5.65
90	K_{I}	19.2	0	/
	K_{II}	472.6	460.2	2.69

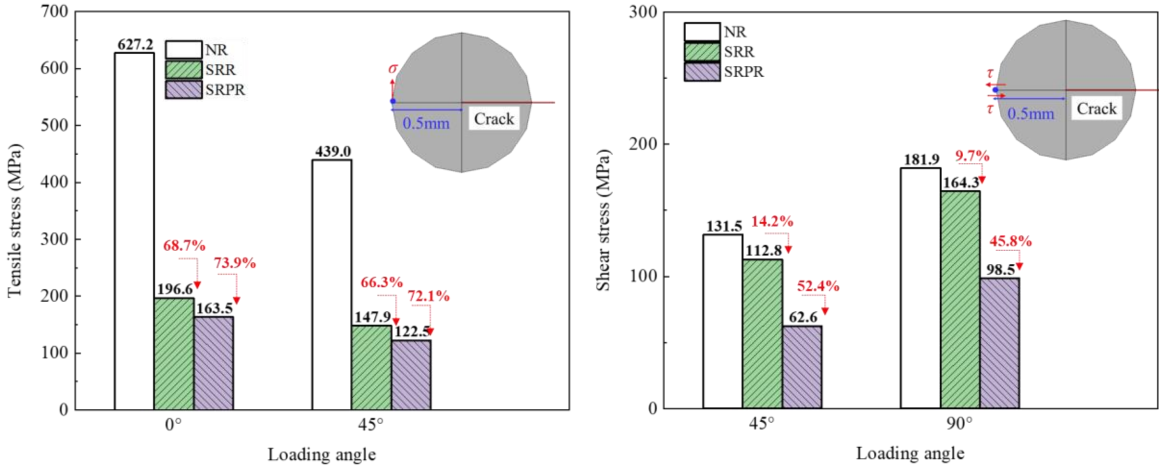

(a) Tensile stresses (b) Shear stresses

Fig. 9 Stresses at the crack tip

2.4.3. Stress characteristics

The stress conditions at the crack tip under various loading angles were investigated. Due to stress singularity, the stress values at the crack tip node tended to approach infinity. Therefore, tensile stresses and shear stresses under 0°, 45°, 90° were extracted at a node located 0.5 mm away from the crack tip, seen in Fig. **9**.

As depicted, both SRR and SRPR were effective in reducing tensile stresses at the crack tip. Compared to SRR, the adoption of SRPR resulted in a further reduction in tensile stress by 5.2% and 5.8% when subjected to pure tension load and tension-shear load mixed load, respectively. Meanwhile, SRR had little effect on reducing shear stress, while SRPR reduced shear stress at the crack tip by nearly half. SRPR achieved a better maintenance effect under shear load, which was consistent with the experimental results.

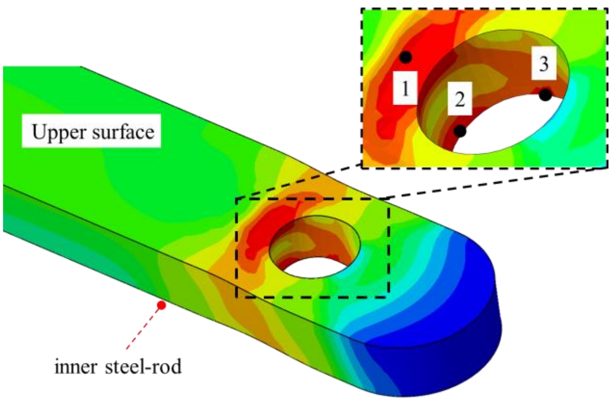

Fig. 10 Mises stress distribution of inner steel-rod

To analyze the stress characteristics of steel-rods under tension-shear mixed load, a force of 100 kN was applied to the model shown in Fig. **8**. The load was incrementally increased from 0 kN to 100 kN in 20 steps, with increments of 5 kN. During the simulation process, notable stress concentrations were observed at both the upper and lower surfaces of inner steel-rod. The locations with high stress concentrations were identified as Point 1, 2, and 3, as illustrated in Fig. **10**, and were potential failure locations for steel-rod.

The mises stress variations at these designated points were extracted, as shown in Fig. **11**. As the applied load increased, the mises stresses also increased, indicating that steel-rod's participation in bearing the load. With further loading, Point 1 yielded, followed by Point 3, while the stress at Point 2 remained relatively low. Upon Points 1 and 3 entered the plastic phase, the stress at Point 2 rapidly increased and reached the yield strength. Point 1 reached the ultimate strength first, leading to damage to the upper surface and failure of steel-rod.

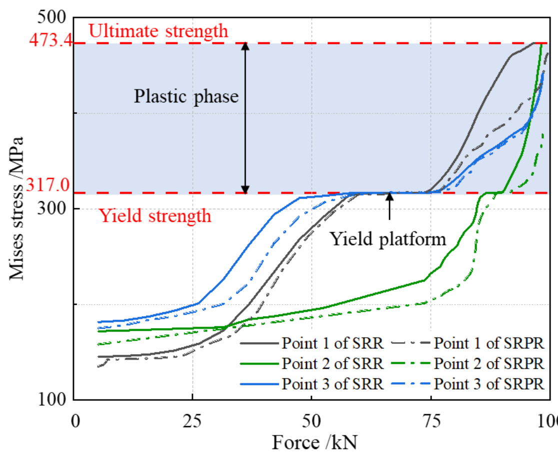

Fig. 11 Stress variation curves of points

It was observed that the stress characteristics at these three points on inner steel-rods of both SRR and SRPR were similar, and steel-rods exhibited similar failure laws, given in Fig. **12**. The overall stresses on inner steel-rod of SRPR were lower than those of SRR. A higher external load on steel-rod of SRPR was required to reach the yield strength.

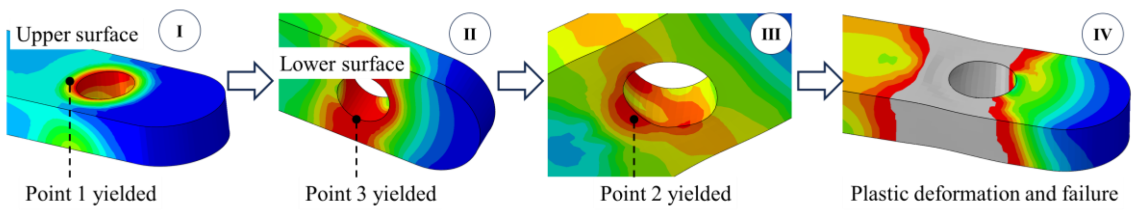

Fig. 12 Failure mode of inner steel-rod

3. Simulation of reinforcement on U-rib

3.1. Segmental model

In the previous study, the roles of SRR and SRPR in hindering crack propagation in flat plate specimens with short cracks was through static testing. Numerical simulations were carried out to evaluate the maintenance effect of these two configurations on long cracks in real bridges. Following the modelling method described in existing research [20], a solid segmental model containing only pavement, deck, U-rid and diaphragm was established by ABAQUS software, as shown in Fig. 13. The overall dimensions of the model were 12 808 × 4 200 × 1 200 mm. The thickness of pavement and deck was 48 mm and 12 mm respectively. The size of the 7 U-ribs was 300 × 6 × 280 mm, they were spaced 700 mm apart and numbered from 1# to 7#. Five diaphragms, each with an 8 mm thickness and 3200 mm space, were labeled from A to E in turn. The elastic modulus of pavement was 1 000 MPa, while that of the rest was 2.06 × 10^5 MPa. The Poisson's ratio of the model was 0.3.

The global grid of the model was 50 mm, and the meshes in the crack region were refined to 2.5 mm. A long crack was inserted in the U-rib-deck weld at the 4# U-rib located between diaphragms B and C, with the crack shape shown in Fig. 14. The cracked body was generated using contour integral method, and twenty degenerative elements were introduced at the crack tip, each with a mesh size of 0.1 mm. All translational degrees of freedom for the deck and diaphragms were restricted. A sub-model containing two U-ribs was created to ensure the accuracy of the calculations.

The load amplitude was determined using Fatigue Load Model III, as specified by the Chinese standard [22]. The spacing between the two lateral axles is 2 000 mm, which exceeds the spacing of three U-ribs. Additionally, the spacing between the second and third axles of the vehicle is 6 000 mm, approximately equivalent to the spacing of three transverse diaphragms. The transverse stress influence line for the orthotropic bridge deck is relatively short [23], so the superimposed stress effects between the lateral axles and the front and rear axles could be disregarded. A biaxial moving load was applied to the model and the distance of front and rear axles was 120 mm. The wheel load area measured 600 × 200 mm with a pressure of 0.5 MPa, as illustrated in Fig. 14.

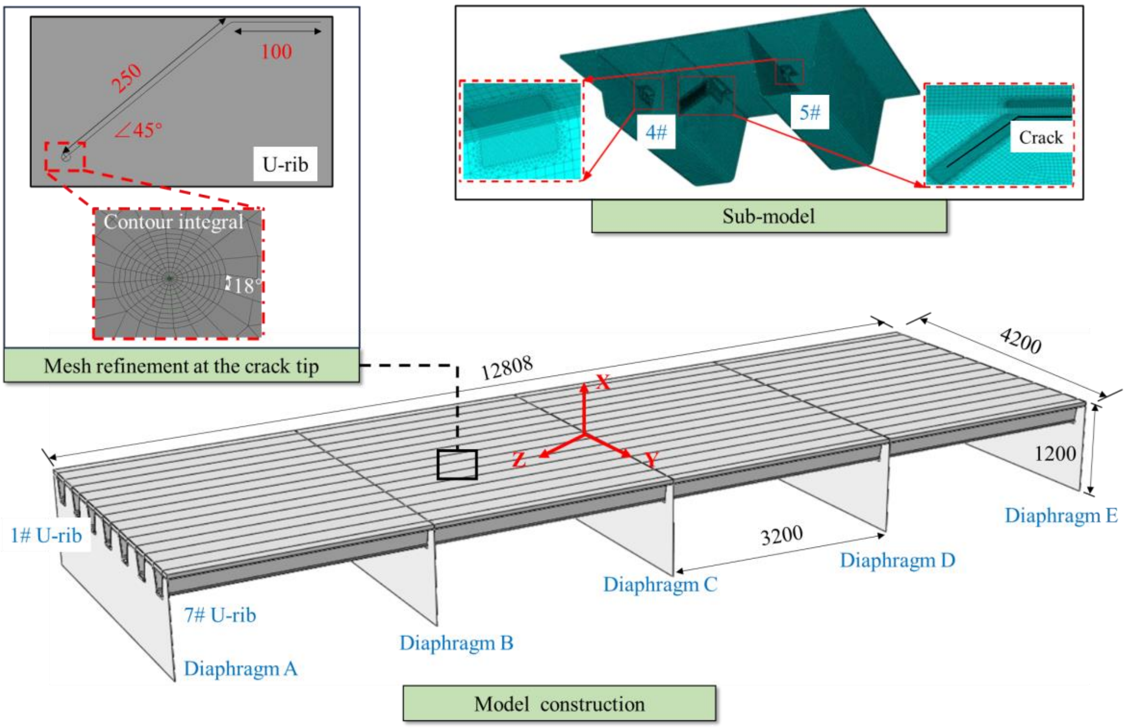

Fig. 13 Segmental finite element model with a long crack (Unit: mm)

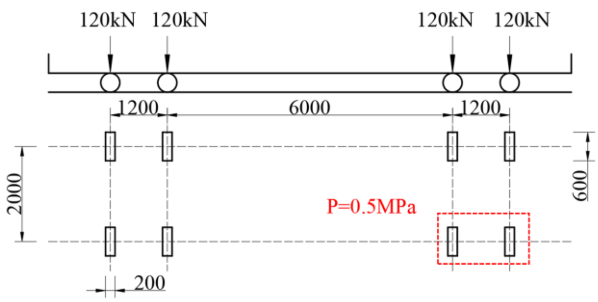

Fig. 14 Load mode (Unit: mm)

3.2. Characteristics of crack

Current practical tests indicate that the most unfavorable working condition is when the vehicle load is directly applied above the crack [24]. Therefore, the biaxial moving load was applied above the long crack mentioned in Fig. 14. The deformation of the crack under this load case was studied. As the crack can be divided into two parts: an oblique crack and a horizontal crack, two local coordinate systems for these two parts were established respectively, seen in Fig. 15, where the x direction represented the out-of-plane direction, and the y direction represented the in-plane direction. Points A and A' were set at the middle of the oblique crack, Points B and B' were set at the ends of horizontal crack. Before loading, Points A and A' coincided, as did Points B and B'. Under the applied loads, mutual extrusion and dislocation were clearly observed. This deformation significantly weakened the mechanical performance and reduced the local stiffness of U-ribs, thereby seriously affecting the structural safety of the steel box girder. Here, the maximum displacement differences in the x and y directions between A and A' were recorded as ΔX_A and ΔY_A, similar to ΔX_B and ΔY_B.

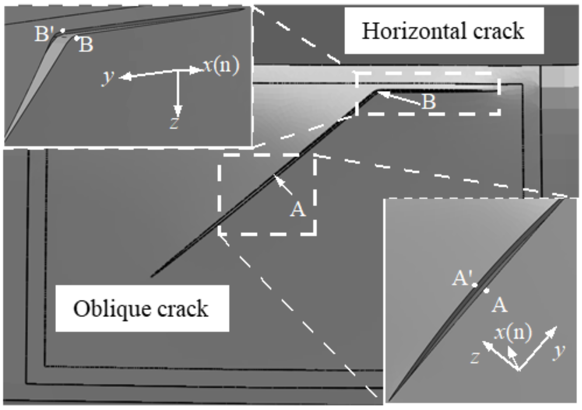

Fig. 15 Deformation of the crack zone

3.3. Reinforcement schemes

Regarding the oblique crack on U-rib as the research object, two reinforcement schemes were proposed: (1) SRR; (2) SRPR. Considering the length of crack, five couples of steel-rods with a 40 mm spacing were arranged on the sub-model, as shown in Fig. **16**a. A 210 × 100 × 6 mm steel plate was positioned over the U-rib crack, with inner steel-rods arranged on the inner side of U-rib, as shown in Fig. **16**c. The materials of steel-rods, steel plate, high strength bolts, spring washers and round shims were specified as Q345qD steel. A pretightening force with the value of 17.8kN was applied on bolts. A friction coefficient of 0.35 was set for the contact surfaces between components.

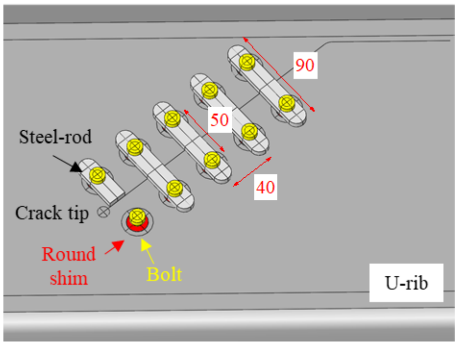

(a) SRR

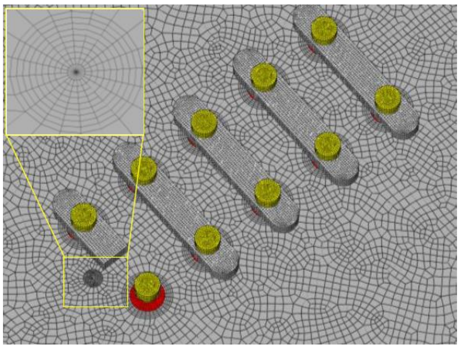

(b) Finite element meshing

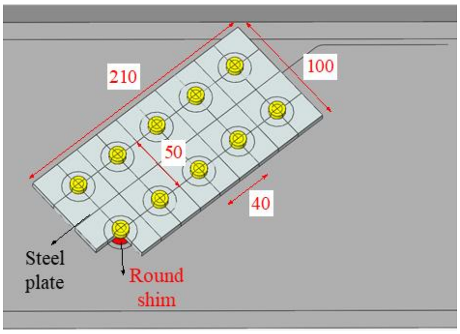

(c) SRPR

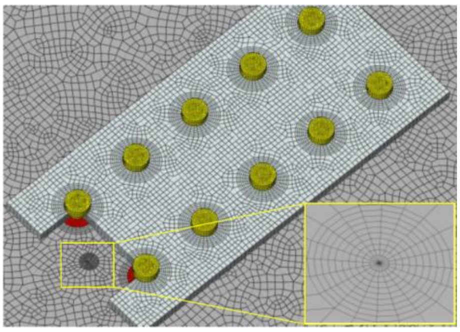

(d) Finite element meshing

Fig. 16 Two reinforcement schemes (Unit: mm)

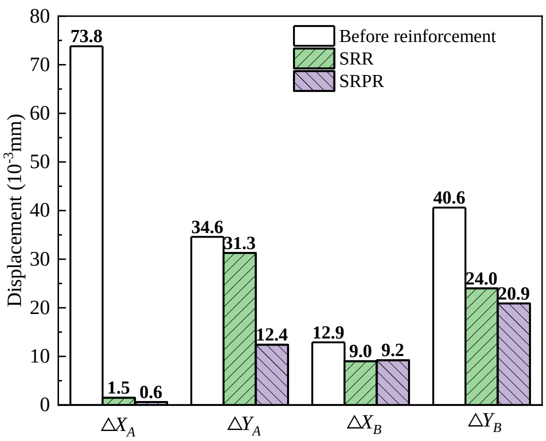

Fig. 17 Maximum displacement differences before and after reinforcement

3.4. Effect Analysis

3.4.1. Deformation

Fig. **17** illustrates the reduction in ΔX_A after applying the SRR and SRPR, resulting in reductions of 98.0% and 99.2%, respectively. These schemes were highly effective in almost completely restraining out-of-plane deformation. For ΔY_A, SRPR reduced it by 64.2%, while SRR only achieved a 9.5% reduction, which indicated that SRPR was more effective at limiting the in-plane deformation of oblique fatigue crack. ΔX_B was small before reinforcement, both of SRR and SRPR could decrease the value of ΔX_B to a certain extent. And ΔY_B was reduced by 40.1% and 48.5% respectively, out-of-plane and in-plane deformation of horizontal crack were limited.

3.4.2. Stress intensity factors

Fig. **18** displays the maximum stress intensity factors on both sides of the crack under the most unfavorable working condition. It was observed that the simulation results for both sides had no significant difference. SRPR and SRR substantially reduce K_I on both sides, providing nearly equal tensile resistance. However, K_{II} was almost unchanged after SRR while it decreased by approximately 35% after SRPR. The steel plate effectively restrained the in-plane deformation of the crack and reduced the concentration of stress at the crack tip. It was shown that SRPR offered superior shear resistance compared to SRR, aligning with the experimental results.

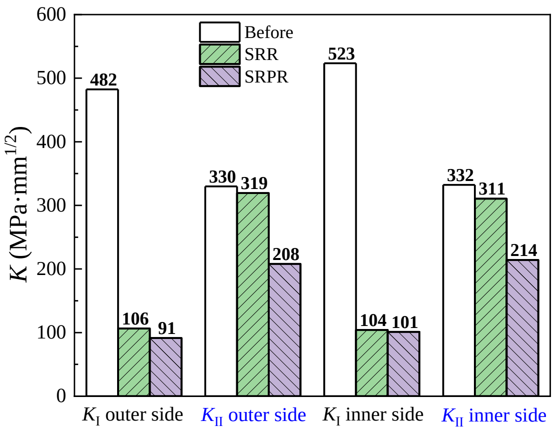

Fig. 18 Maximum K at two sides of crack under Load Case T6

4. Field maintenance and monitoring

4.1. Project of field monitoring

The simulation results indicate that the use of steel-rods and steel plates demonstrated excellent shear resistance, proving to be an effective solution for retrofitting long fatigue cracks in U-ribs. To study the maintenance effect in real bridge, field reinforcement and monitoring were conducted. The background bridge is a steel box girder suspension bridge with a main span exceeding 1,300 meters, which has been in operation for over 20 years. The average daily traffic volume on the bridge has surpassed 100,000 vehicles. The increasing traffic volume has contributed to significant fatigue problems. The fatigue crack in question initiated from the weld joint of U-rib, then forked and propagated obliquely along the U-rib base metal. As vehicle passed over the crack, obvious dislocations were observed on the surface. The length of the crack on the base metal surface was approximately 180mm. Fig. **19** gives the strengthening scheme.

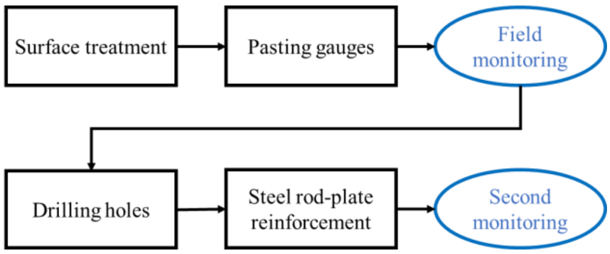

Fig. 19 Scheme of construction

Before attaching the strain gauges, the surface underwent polishing to remove the coating. Six holes, each with 18 mm diameter, were drilled on double sides of the crack body by magnetic drill, as depicted in Fig. **20**b. The strain gauges were installed in a vertical arrangement following the crack tip. To ensure comprehensive maintenance that considered operational constraints and the specific crack characteristics, steel-rods and steel plate were utilized simultaneously, seen in Fig. **20**c. The strain data near the crack tip was recorded using a strain indicator operating at a frequency of 256Hz, and the strain records are converted into stresses by using Hooke's law $\sigma = E\varepsilon$. For the material of steel box girder in the studied bridge, the Young's modulus E is 2.10×10^5MPa, and the Poisson's ratio is 0.3. Data acquisition occurred over a 1-hour period both before and after maintenance.

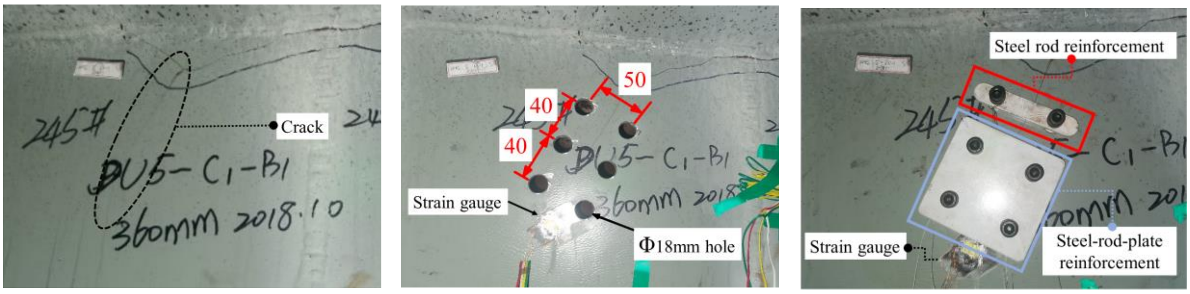

(a) Before maintenance (b) Drilling holes (c) After maintenance

Fig. 20 Diagram of reinforcement in real bridge

4.2. Stress range spectrum

The stress range spectrum, which was based on collected strain data, underwent analysed. To calculate the stress range spectrums, the rain-flow counting method [25] was employed for processing the stress data. After rain-flow computation, the final stress range spectrum is presented in Fig. **21**.

The stress range spectrum for a 1-hour duration was analysed based on the obtained data. The stress amplitudes below 5MPa were excluded from consideration, as the low-stress random amplitudes made only a minimal contribution to the fatigue damage, which were mainly caused by other factors, such as wind, temperature gradient, etc. It was observed that the number of cycles at high stress ranges decreased obviously after maintenance, while the low stress ranges increased. The maximum tensile-compressive stress amplitude reduced from 70 MPa to 50 MPa, marking a 28% decrease. Additionally, the maximum shear stress amplitude reduced from 80 MPa to 60 MPa, with a fall of 25%. These results clearly indicated the positive impact of the maintenance.

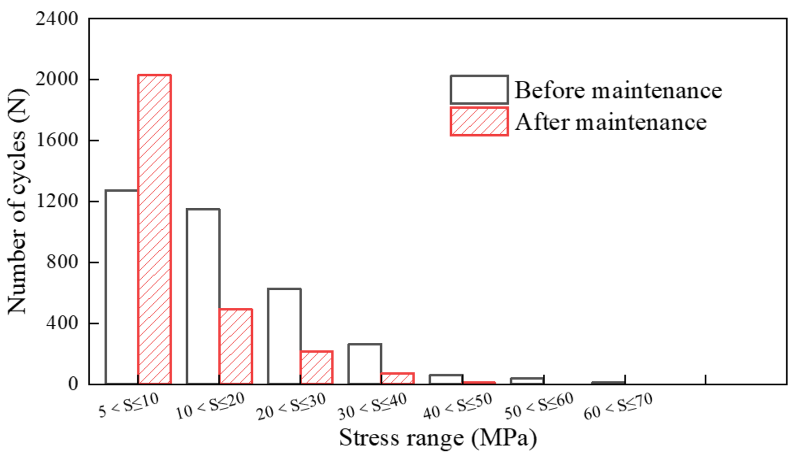

(a) Tensile and compressive stress range spectrum

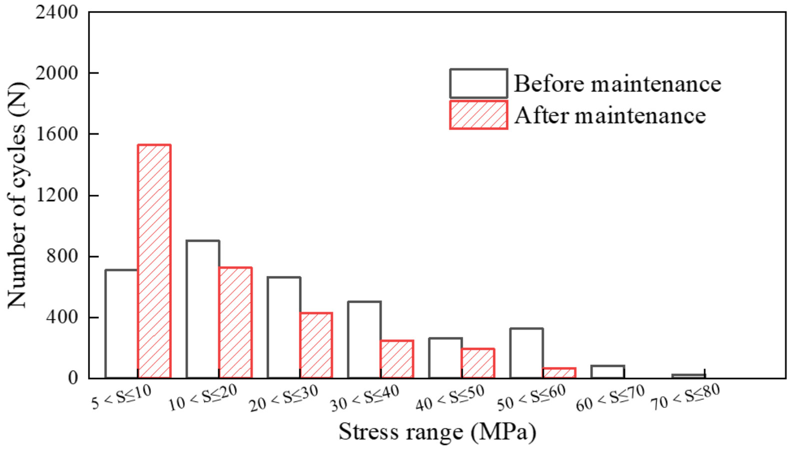

(b) Shear stress range spectrum

Fig. 21 Stress range spectrums obtained within 1 hour

5. Conclusions

(1) Both steel-rod reinforcement (SRR) and steel-rod-plate reinforcement (SRPR) significantly enhanced tensile capacity. Under tension load, these two configurations relieved the stress concentration and reduced K_I. When subjected to a tension-shear mixed load, SRR exhibited minimal shear resistance, whereas SRPR demonstrated a more substantial shear performance. The steel-rods have similar stress characteristics and damage forms, which were manifested by the hole edge reaching yield and plastic damage.

(2) SRPR effectively constrained both out-of-plane and in-plane deformations of oblique cracks in U-rib-to-deck welded joint, reducing the stress intensity factors at the crack tip. While SRR had limited effectiveness in preventing crack deformation.

(3) As indicated by the analysis of the real bridge monitoring results, the method that using steel-rods and steel plates improved the stress conditions at the crack tip. A significant reduction in the number of cycles at high tensile and shear stress ranges was observed, while an increase in the cycles at low stress ranges occurred. As a result, the fatigue crack propagation was effectively suppressed.

Acknowledgements

The research reported herein has been conducted as part of the research projects granted by the National Natural Science Foundation of China under (Grant No. 52308166 and 52378153), the Fundamental Research Funds for the Central Universities under (Grant No. B230201034 and B230204003). The assistances are gratefully acknowledged.

References

[1] Fisher, J.W. and Roy, S., "Fatigue of steel bridge infrastructure", Structure and Infrastructure Engineering, 7, 457-475, 2011. https://doi.org/10.1080/15732479.2010.493304
[2] Jong, F.B.P., "Overview fatigue phenomenon in orthotropic bridge decks in The Netherlands", 2004 Orthotropic Bridge Conference, Sacramento, 489-512, 2004.
[3] Gao, T., Yuanzhou, Z.Y., Ji, B.H. and Xie, Z., "Vision-based fatigue crack automatic perception and geometric updating of finite element model for welded joint in steel structures", Computer-aided Civil and Infrastructure Engineering, 1-17, 2024. https://doi.org/10.1111/mice.13166
[4] Patel, A.B. and Pandey, R.K., "Fatigue crack growth under mixed-mode loading", Fatigue & Fracture of Engineering Materials & Structures, 4(1), 65-77, 2007.
[5] Fang, L., Fu, Z.Q., Ji, B.H. and Kainuma, S., "Research on mixed mode crack drilling under out-of-plane shear in steel bridge deck", International Journal of Fatigue,156, 106679, 2022. https://doi.org/10.1016/j.ijfatigue.2021.106679
[6] Yao, Y., Ji, B.H., Fu, Z.Q., Zhou, J. and Wang, Y.X., "Optimization of stop-hole parameters for cracks at diaphragm-to-rib weld in steel bridges", Journal of Constructional Steel Research, 162, 105747,2019. https://doi.org/10.1016/j.jcsr.2019.105747
[7] Gong, H., Jin, Z.G., Yang, F.P., and Mao, W.T., "Analysis of stop-hole effects on mode I-II fatigue crack behavior for Q420 steel using experiments, FEM and variable length RNN approaches", Theoretical and Applied Fracture Mechanics, 124, 103823, 2023. https://doi.org/10.1016/j.tafmec.2023.103823
[8] Yamada, K., Ishikawa, T. and Kakiichi, T., "Rehabilitation and improvement of fatigue life of welded joints by ICR treatment", Advanced Steel Construction. 11(3), 294–304, 2015. https://doi.org/10.18057/IJASC.2015.11.3.4
[9] Yuanzhou, Z.Y., Ji, B.H., Fu, Z.Q., Kainuma, S. and Tsukamoto, S., "Fatigue crack retrofitting by closing crack surface", International Journal of Fatigue. 119(Feb), 229-237, 2019. https://doi.org/10.1016/j.jcsr.2017.12.015
[10] Yuanzhou, Z.Y., Ji, B.H., Wang, Q.D., and Fu, Z.Q., "Investigation on crack behaviours by closing its surface using impact treatment", Journal of Constructional Steel Research, 156 (May), 1-8, 2019. https://doi.org/10.1016/j.jcsr.2019.01.009
[11] Miki, C., "Fatigue damage in orthotropic steel bridge decks and retrofit works", International Journal of Steel Structures, 6(4), 255-267, 2006.
[12] Fu, Z.Q., Wang, Q.D., Ji, B.H. and Yuanzhou, Z.Y., "Rewelding repair effects on fatigue cracks in steel bridge deck welds", Journal of Performance of Constructed Facilities, 31(6), 04017094, 2017. https://ascelibrary.org/doi/10.1061/%28ASCE%29CF.1943-5509.0001083
[13] Jiang, F., Ding, Y.L., Song, Y.S., Geng, F.F. and Wang, Z.W., "CFRP strengthening of fatigue cracks at U-rib to diaphragm welds in orthotropic steel bridge decks: Experimental study, optimization, and decision-making", Structures, 43, 1216-1229, 2022. https://doi.org/10.1016/j.istruc.2022.07.039
[14] Wang, C.S, Zhai, M.S., Duan, L. and Wang, Y.Z., "Cold reinforcement and evaluation of steel bridges with fatigue cracks", Journal of Bridge Engineering, 23(4), 04018014, 2018. https://doi.org/10.1061/(ASCE)BE.1943-5592.0001219
[15] Meng. C., Yuanzhou, Z.Y., Ji. B.H., Chen, Z.Z. and He, B., "Static analysis on fatigue crack retrofitting using steel-rod reinforcement method", Thin-Walled Structures, 198, 111687, 2024. https://doi.org/10.1016/j.tws.2024.111687
[16] Richard, H.A. and Benitz, K., "A loading device for the creation of mixed mode in fracture mechanics", International Journal of Fracture, 22,55–58, 1983. https://doi.org/10.1007/BF00942726
[17] Rittel, D., "A hybrid experimental-numerical investigation of dynamic shear fracture", Engineering Fracture Mechanics. 72(1), 73-89, 2005. https://doi.org/10.1016/j.engfracmech.2004.01.013
[18] Zhou, G.P. and Chen. H., "Influence of strain gauge position on the calculation of dynamic stress intensity factors", Journal of Harbin Engineering University, 41(12) 1772-1778, 2020. (in Chinese). http://dx.doi.org/10.11990/jheu.201906086
[19] Wright, W.J., "Fracture toughness requirements for highway bridges: past and future trends", Progress in Structural Engineering and Materials, 4(1) 96-104, 2010. https://doi.org/10.1002/pse.99
[20] Richard, H.A., "Some theoretical and experimental aspects of mixed mode fractures", Proceedings of the 6th International Conference on Fracture, New Delhi, India, 3337-3344, 1984.
[21] Fu, Z.Q., Ji, B.H., Ye, Z. and Wang, Y.X., "Fatigue evaluation of cable-stayed bridge steel deck based on predicted traffic flow growth", KSCE Journal of Civil Engineering, 21(4), 1400-1409, 2017. https://doi.org/10.1007/s12205-016-1033-0
[22] Ministry of Transport of the People's Republic of China, Specifications for Design of Highway Steel Bridge: JTG-D64, 2015. (In Chinese).
[23] Ji, B.H., Chen, X., Liu, R. and Yang, M.Y., "A numerical study on the fatigue effect of trough-deck plate weld joint to steel bridge deck system", Progress in Steel Building Structures, 16(6), 56-62, 2014. (In Chinese). https://doi.org/10.13969/j.cnki.cn31-1893.2014.06.007
[24] Wang, Y.X., Fu, Z.Q., Ge, H.B., Ji, B.H. and Hayakawa, N., "Cracking reasons and features of fatigue details in the diaphragm of curved steel box girder", Engineering Structures, 201, 109767, 2019. https://doi.org/10.1016/j.engstruct.2019.109767
[25] Matsuiski, M. and Endo, T., "Fatigue of metals subjected to varying stress", Japan Society of Mechanical Engineering, 96, 100-103,1968.